Imaging properties of finite-size left-handed material slabs

Jianbing J. Chen, Tomasz M. Grzegorczyk, Bae-Ian Wu, and Jin Au Kong
Research Laboratory of Electronics and Department of Electrical Engineering and Computer Science, Massachusetts Institute of Technology, Cambridge, Massachusetts 02139-4307, USA
(Received 1 July 2006; published 24 October 2006)

Finite-size left-handed material (LHM) slabs are studied both analytically and numerically. The analytical method is based on Huygens' principles using truncated current sheets that cover only the apertures of the slabs. It is shown that the main effects on the images' spectra due to the size of the slabs can be predicted by the proposed analytical method, which can, therefore, be used as a fast alternative to the numerical simulations. Furthermore, the property of negative-energy streams at the image plane is explained. This unique property is found to be due to the interactions between propagating and evanescent waves and can only occur with LHM slabs, both finite size and infinite.

DOI: 10.1103/PhysRevE.74.046615 PACS number(s): 41.20.−q, 42.25.−p

I. INTRODUCTION

The concept of using a left-handed material (LHM) slab, in which the real part of the material's permittivity and permeability are negative, as a flat lens was introduced by Veselago [1], who showed that the propagating waves from a source can be focused by the LHM slab. Building upon this idea, Pendry [2] further demonstrated theoretically that a perfectly matched LHM slab can also amplify evanescent waves, therefore restoring the entire spectrum of the source at the image plane to obtain a so-called prefect resolution. Even though practical limitations, such as losses in the material and the mismatch in material properties [3,4] prevent the realization of a perfect resolution imaging system using an LHM slab, images with subwavelength resolution have been obtained by numerical simulations [5–8] and confirmed by experimental measurements [9,10]. These studies suggest that LHM slabs have a great potential to be used for imaging applications with a better resolution than conventional lenses. In practical systems the slab's size is finite. However, there have been only a few studies, either theoretically, numerically, or experimentally, on the effect of the finiteness of the LHM slabs on the resolution power of the lens. Among the properties of the finite-size slabs people have come to know, an interesting one is that the image quality is not sensitive to the size of the finite slab [9], which is contrary to a conventional lens. In addition, a peculiar property that negative energy streams can appear at the image plane with a finite-size slab was discovered [11]. Yet, no satisfactory explanations of these properties have been reported in the literature. We address this need by analyzing these properties using analytical methods combined with numerical simulations, which allow us to provide a series of physical explanations to the imaging properties of finite-size LHM slabs. In Sec. II, the equivalent current sheet method from Huygens' principle is applied to study the imaging capability of the finite-size slabs. The main features in the image spectrum due to the slab's finite length are explained by considering the changes in fields at the LHM slab boundary. In Sec. III, the energy stream at the image plane is investigated by decomposing a line source into plane waves, i.e., propagating and evanescent waves, and evaluating the energy contributions from the wave interactions. In doing so, we show that the negative-energy stream is a not only a property of finite-size LHM slabs but also a property of infinite LHM slabs. Finally, the last section gives a conclusion to the paper.

II. IMAGE SPECTRUM IN THE FINITE LHM SLAB IMAGING SYSTEM

In order to evaluate an imaging system, the knowledge of the image spectrum is important. For an infinite LHM slab, the image spectrum can be obtained analytically, therefore the resolution can be found readily by locating the maximum wave number in the spectrum. When the LHM slabs become finite, it has been found that the image resolution is not affected noticeably, although the image spectrum changes [9]. In the first part of the present paper, we analyze how the image spectrum changes with the slab's length and how the maximum wave number is affected, thus providing an explanation to the observation reported in Ref. [9]. Since a finite-size slab does not have a geometry that can define a coordinate system in which the Maxwell's equations can be easily expanded (e.g., like spheres, cylinders, etc.), we resort to an approximation method, which consists in studying the electric and magnetic fields at the slab's second boundary (image side) instead. From Huygens' principle, the fields at the slab's boundary can be converted into equivalent current sheets, which can in turn be used to find the fields at the image plane. By observing the fields at the slab boundary, the changes in the image fields can be found, and subsequently the spectrum can be determined.

We shall first start with an infinite slab. The setup of the LHM slab imaging system is shown in Fig. 1: a line source (infinite in $\hat{y}$) is placed at $x=d_1$ in the x-z plane; a slab along $\hat{z}$ with thickness d_s is located between the coordinates $x=0$ and $x=d_2=-d_s$. For simplicity, we choose $d_1=-3d_s/2$ so that the image plane is at $x=d_3=d_s/2$. The length L depicted in Fig. 1 is infinite in this case.

The electric fields from a line source can be expressed in the plane-wave representation as

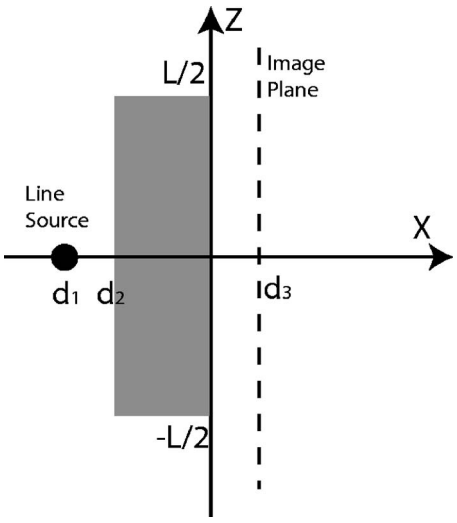

FIG. 1. Geometry of the LHM slab imaging system.

$$\bar{E}_{ln}(x,z) = \hat{y}\frac{-\omega\mu_o}{4}H_0^{(1)}(k_o|\rho-\rho'|)$$
$$= \hat{y}\frac{-\omega\mu_o}{4\pi}\int_{-\infty}^{\infty} dk_z \frac{1}{k_x} e^{ik_x(x-d_1)}e^{ik_z z}. \quad (1)$$

After the transmission through the slab, the tangential fields at the slab's second boundary are

$$E_y(z) = \frac{-\omega\mu_o}{4\pi}\int_{-\infty}^{\infty} dk_z \frac{T(k_z)}{k_x} e^{-ik_x d_1}e^{ik_z z}, \quad (2)$$

$$H_z(z) = \frac{-1}{4\pi}\int_{-\infty}^{\infty} dk_z T(k_z) e^{-ik_x d_1}e^{ik_z z}, \quad (3)$$

where $T(k_z)$ is the transmission coefficient of the slab, $k_o^2 = k_x^2 + k_z^2 = \omega^2\mu_o\epsilon_o$ is the free-space wave vector. The fields at the image plane are then obtained from those at the slab boundary. Applying the integral formulation of Huygens' principle [12], the field beyond the slab's boundary ($x>0$) can be written as

$$\bar{E}(x,z) = \int_{z'} dz' \{i\omega\mu_o[\hat{n}\times\bar{H}(\bar{r}')]g(\bar{r},\bar{r}')$$
$$+ [\hat{n}\cdot\bar{E}(\bar{r}')]\nabla' g(\bar{r},\bar{r}') + [\hat{n}\times\bar{E}(\bar{r}')]\nabla' g(\bar{r},\bar{r}')\}, \quad (4)$$

where the usual surface integral has been replaced by a line integral along $\hat{z}$ because of the invariance of the geometry along $\hat{y}$. $\bar{E}(\bar{r}')$, $\bar{H}(\bar{r}')$ are the fields at the slab's second boundary, which are expressed in Eqs. (2) and (3); $\hat{n}=\hat{x}$ is the normal of the boundary. The Green's function is $g(\bar{r},\bar{r}') = (i/4)H_0^{(1)}(k_o|\bar{\rho}-\bar{\rho}'|)$ and the integration is along z. Plugging in the expression of the fields, we find

$$\bar{E}(x,z) = \hat{y}\int_{-\infty}^{\infty} dz' \frac{i\omega\mu_o}{4\pi}\int_{-\infty}^{\infty} dk_z T(k_z) e^{-ik_x d_1}e^{ik_z z'}$$
$$\times \frac{i}{4}H_0^{(1)}[k_o\sqrt{(z-z')^2+x^2}]$$
$$+ \hat{y}\int_{-\infty}^{\infty} dz' \frac{-\omega\mu_o}{4\pi}\int_{-\infty}^{\infty} dk_z \frac{T(k_z)}{k_x} e^{-ik_x d_1}e^{ik_z z'}$$
$$\times \frac{\partial}{\partial x'}\frac{i}{4}H_0^{(1)}[k_o\sqrt{(z-z')^2+(x-x')^2}]\Big|_{x'=0}$$
$$= \hat{y}E_1 + \hat{y}E_2, \quad (5)$$

where E_1 and E_2 are the two integrals, respectively. It is straightforward to show that $E_1=E_2$, indicating that the fields generated from the electric-current sheet are the same as the ones from the magnetic-current sheet. Finally, the spectrum of the image is obtained by applying the inverse Fourier transform of $E(x=d_3,z)$, from which we get

$$E(k_z) = \int_{-\infty}^{\infty} dz 2E_1(x=d_3,z)e^{-ik_z z}$$
$$= \frac{-\omega\mu_o}{4\pi}\frac{e^{ik_x d_3}}{k_x}T(k_z)e^{-ik_x d_1} \quad (6)$$
$$= \frac{-\omega\mu_o}{4\pi}\frac{e^{ik_x d_3}}{k_x}T_1(k_z), \quad (7)$$

where $T_1(k_z)=T(k_z)\exp(-ik_x d_1)$. It can be seen that the spectrum of the image can be interpreted as the spectrum of the line source multiplied by the slab's transmission coefficient with a phase propagation term.

With the procedure established for the infinite slab, we pursue with the study of the finite-size slab. For the general discussion, we write the field equation at the finite slab boundary as

$$\bar{E}_f(z) = \hat{y}\frac{-\omega\mu_o}{4\pi}f(z)\int_{-\infty}^{\infty} dk_z \frac{T(k_z)}{k_x} e^{-ik_x d_1}e^{ik_z z}, \quad (8)$$

where the function $f(z)$ represents the change in the field due to the finite size when compared to the infinite slab case. In what follows, we make the approximation $f(z)=0$ for $z<-L/2$ or $z>L/2$, which indicates that the current sheet can be viewed as from an aperture of size equal to the size of the slab.

This assumption has been validated by numerical simulations, which show that the fields at the slab's boundary are much stronger than the fields in free space. As an example, we consider a slab of thickness $d_s = 0.2\ \lambda$ and of length $L=2\lambda$, which yields an aspect ratio similar to those used in practical applications. In Fig. 2, we compare the fields at the image plane from the full-wave numerical simulation and the fields calculated using the equivalent currents from only the fields at the slab's boundary (i.e., with the finite aperture effect). It is evident that the contributions from only the fields at the slab's boundary are almost equivalent to the contribution of the total field. The difference in the peak

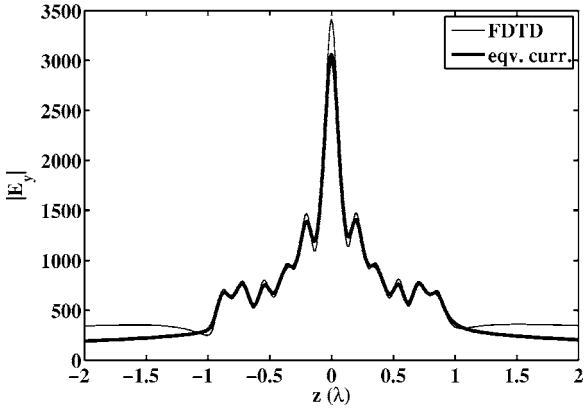

FIG. 2. E field at the image plane approximated by the current sheet compared with the E field from the FDTD (without approximation). The current sheet spans only the aperture of the finite slab. The slab has a thickness $d_s=0.2\lambda$ and a length of $L=2\lambda$. The property of the slab is $\mu_r=\epsilon_r=-1.0003$. It can be seen that the current sheet method is a valid approximation method for estimating the fields at the image plane.

magnitudes does not affect the image resolution since the 3 dB width of the fields from both results are very close.

Following the same procedure as the one used to obtain Eq. (5), the electric field at the image plane ($x=d_3$) is obtained as

$$E(z)=\frac{-\omega\mu_o}{8\pi^2}\int_{-\infty}^{\infty}dk_z'T(k_z')e^{-ik_x'd_1}\int_{-\infty}^{\infty}dk_z''\frac{e^{ik_x''d_3}}{k_x''}e^{ik_z''z}F(k_z'-k_z''), \tag{9}$$

where $F(k_z)$ is the Fourier transform of $f(z)$. The spectrum of the electric field at the image plane can be evaluated as

$$\begin{aligned}E(k_z)&=\frac{-\omega\mu_o}{8\pi^2}\int_{-\infty}^{\infty}dk_z'T(k_z')e^{-ik_x'd_1}\\&\quad\times\int_{-\infty}^{\infty}dk_z''\frac{e^{ik_x''d_3}}{k_x''}F(k_z'-k_z'')2\pi\delta(k_z''-k_z)\\&=\frac{-\omega\mu_o}{4\pi}\frac{e^{ik_xd_3}}{k_x}\int_{-\infty}^{\infty}dk_z'T(k_z')e^{-ik_x'd_1}F(k_z'-k_z)\\&=\frac{-\omega\mu_o}{4\pi}\frac{e^{ik_xd_3}}{k_x}\{T_1(k_z)\otimes F(k_z)\},\end{aligned} \tag{10}$$

where the $\otimes$ is the convolution operator. Equation (10) indicates that the image spectrum from a finite-size slab can be approximated by the convolution of the transmission coefficient and the Fourier transform of $f(z)$ multiplied by the line-source spectrum. Since the image resolution is closely tied to the spectrum, Eq. (10) is also useful for the study of image resolution. The next important step is to determine what function should be used for $f(z)$.

Since $f(z)$ relates to the field changes at the slab's boundary, we plot in Figs. 3 and 4 the electric field's amplitude and phase at the boundary from the infinite slab and the finite slab, respectively. The field from the infinite slab is obtained

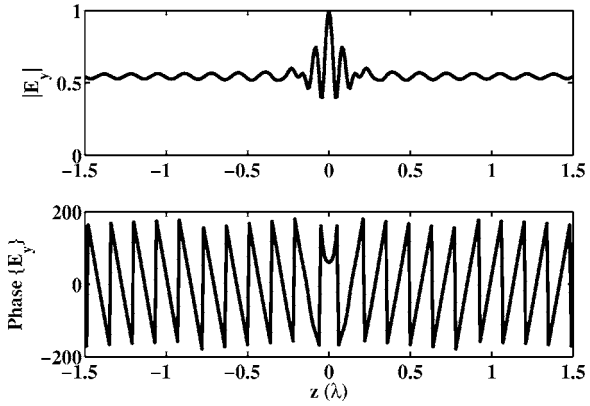

FIG. 3. Amplitude and phase of the E field at the infinite slab boundary. The slab has a thickness of $d_s=0.2\lambda$.

by evaluating Eq. (2), while the field from the finite slab is obtained by numerical simulation using the finite-difference time domain (FDTD) method. Both slabs have a thickness $d_s=0.2\lambda$ and the finite slab has a length of $L=2\lambda$. In choosing the material properties for the infinite slab, we make use of our previous effort [8], which points out the inherent mismatch in material due to the finite discretization in the FDTD for implementing a frequency-dispersive model (e.g., Drude model). Hence we use $\mu_r=\epsilon_r=-1.0003$ for the slab, which is equivalent to the LHM slab implemented in the FDTD using $\Delta=\lambda/100$ and the corresponding time step.

Examining both amplitudes in Figs. 3 and 4, one can observe that in the case of the finite slab, the fields taper off at the edge of the slab, while in the case of infinite slab the fields maintain a constant but small oscillation. Checking the phase of these two cases, one can realize that the phases are almost identical within the slab's length. This is not a coincidence. In the case of the infinite slab, studies [6,13] show that the field at the slab's boundary is dominated by the contribution from the pole in the transmission coefficient $T(k_z)$ as the result of the contour integration in the complex plane for Eq. (2). The wave number where the pole occurs approximately corresponds to the resolution of the slab. Since the pole contributes to a single dominating surface

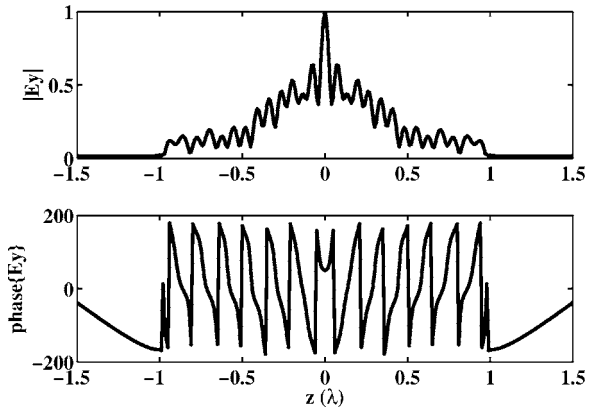

FIG. 4. Amplitude and phase of the E field at the finite slab boundary. The slab has a thickness of $d_s=0.2\lambda$ and a length of $L=2\lambda$.

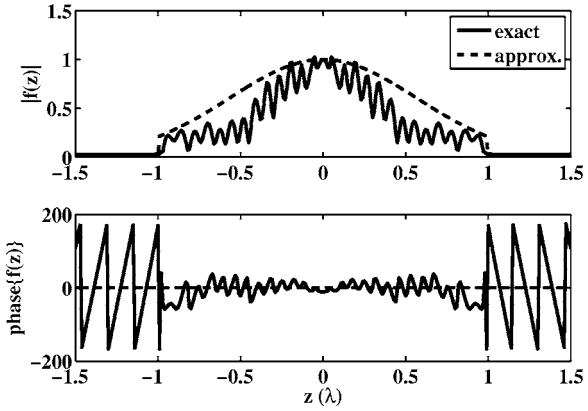

FIG. 5. Amplitude and phase of the function $f(z)$. The exact $f(z)$ is obtained from the FDTD simulations, and the approximated $f(z)$ is a truncated Gaussian function.

wave propagating at the slab boundary, the phase of the field is determined by this surface wave mode. In the case of the finite slab, the contribution from the pole is still significant at the boundary so that the phase propagation remains almost the same. By taking the ratio of the fields, one can find the exact function for $f(z)$, which is shown in Fig. 5 for both the amplitude and the phase. In the region of the slab's length, the tapering amplitude and near-zero phase can be readily seen. In addition, we can obtain the image spectra (normalized to the line-source spectrum) from both slabs, and the comparison is shown in Fig. 6. We see that the position of the main peak (due to the pole) remains unchanged except for a smaller amplitude in the finite slab case. Furthermore, there are oscillations in the band for the finite slab.

In order to understand these changes in the spectrum, we shall now proceed with the approximation of $f(z)$. This is a necessary step to reveal the physical interpretation of the finite slab's image spectrum. Based on the above discussion, we propose to approximate $f(z)$ as a real function with Gaussian tapered amplitude $\exp(-z^2/g^2)$ but truncated at the slab boundary. The plot of the approximated $f(z)$ is shown by

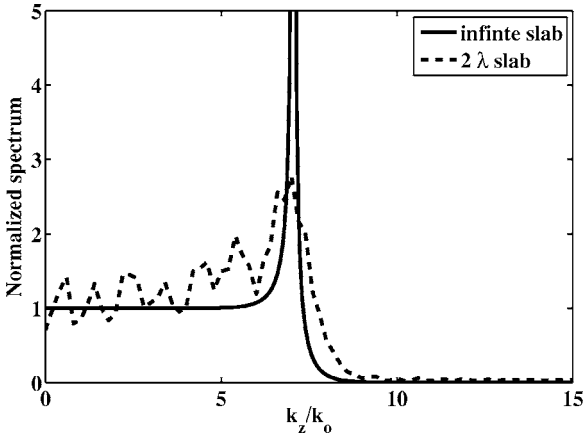

FIG. 6. Spectrum of the E field at the image plane from an infinite slab and a finite slab. In both cases, slabs have a thickness of $d_s=0.2\lambda$. The finite slab has a length of $L=2\lambda$. The spectrum is normalized to the line-source spectrum.

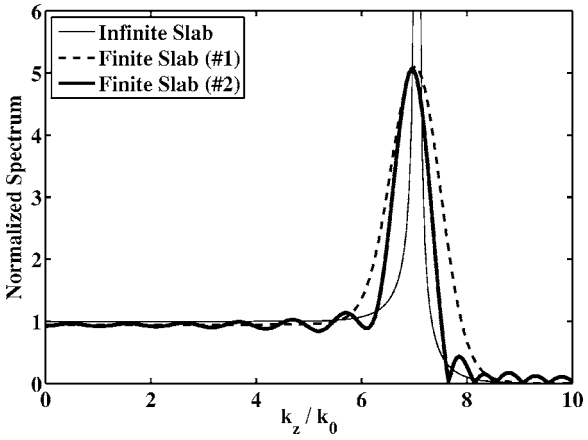

FIG. 7. Spectrum of the E field at the image plane from an infinite slab and the approximated spectrum from a finite slab. The slabs are the same as in Fig. 6. Approximation method No. 1 is to use the Gaussian function for the current sheet. Method No. 2 is to use the Gaussian function truncated to the slab aperture.

the dashed line in Fig. 5. After the approximation, Eq. (10) can be used to evaluate the image spectrum without the aid of numerical simulation. The proposed $f(z)$ approximation has two features, i.e., a Gaussian amplitude and a truncation at the slab's edge. We study the effect of these features independently. Figure 7 shows the image spectrum with $f(z)$ as a Gaussian function with and without the truncation. Compared with the spectrum from the infinite slab, the Gaussian approximation produces the same shape with a lower peak amplitude and wider peak width. This is well expected as the consequence of convolution operation with a Gaussian function. Notice that no oscillation is introduced into the spectrum. With $f(z)$ approximated as truncated Gaussian function, the spectrum exhibits additional oscillations in the spectrum as shown in the figure and the periodicity agrees with the one obtained from the simulations (Fig. 4). It can therefore be concluded that the periodicity comes from the length of the slab. The differences in amplitudes between the approximated spectrum and the actual one are due to the simplification of the actual $f(z)$. However, these differences do not prevent us from observing the main features in the image spectrum. By reducing the length of the slab from infinite to finite, the image spectrum is changed with a lower main peak amplitude and an oscillation within the band, but these changes do not reduce the maximum wave number in the image spectrum. Hence the size of the LHM slabs has little effect on the image resolution. The experimental observation that subwavelength imaging can be achieved by small-size slabs and that increasing the slab's size does not make significant improvements in the image resolution [10] is thus explained. We shall note that this conclusion only applies to LHM lenses, which in principle operate in the near field.

III. NEGATIVE ENERGY IN THE LHM SLAB IMAGING

In addition to the property of preserving the image resolution as discussed in the previous section, another unique

property reported with LHM slabs is the negative energy stream at the image plane. This property has been emphasized in the case of finite slabs in Ref. [11]. For a conventional lens imaging system, the energy at the image plane is always in the positive direction, i.e., in the propagating direction of the waves emitted from the source. For LHM flat-lens imaging systems, however, there exist regions at the image plane where the energy streams are in the negative direction, even though the energy is positive at the focal point. We show here that not only this phenomenon is not peculiar, but also it is still present in the case of infinite slabs. In order to facilitate the discussion, we shall analyze the infinite slab case first, then continue on discussing the case of the finite LHM slabs.

Equation (1) shows that a line source consists of propagating waves as well as evanescent waves. It is also known that each individual propagating wave carries power in the forward direction after transmitting through the slab, while evanescent waves carry no power in the forward direction. Therefore it is obvious that the negative energy stream cannot be explained by just considering each individual wave component. Considering the interactions between the waves, there exist three different cases of interaction: (i) interaction between propagating waves, (ii) between evanescent waves, and (iii) between propagating and evanescent waves.

For the first case, taking two propagating waves (TE polarized) as $E_{y\eta}=E_o \exp\{ik_{x\eta}x+ik_{z\eta}z\}$, where $\eta=a,b$ for the two waves and $k_\eta^2=k_{x\eta}^2+k_{z\eta}^2=\omega^2\mu_1\epsilon_1$, the total time-averaged Poynting power in $\hat{x}$, which is the forward direction of the imaging system, can be written as

$$\langle S_x\rangle = \frac{1}{2}E_o^2\left[\left(\frac{k_{xa}}{\omega\mu_1}+\frac{k_{xb}}{\omega\mu_1}\right)\{1+\cos[(k_{xa}-k_{xb})x + (k_{za}-k_{zb})z]\}\right], \quad (11)$$

where $\langle\ \rangle$ indicates the time average. It is clear that $\langle S_x\rangle>0$, which means that the interactions between propagating waves always contribute to a positive power. For the second case, taking two evanescent waves with $E_{y\eta}=\exp\{ik_{z\eta}z-\alpha_{x\eta}x\}$, we get

$$\langle S_x\rangle = \sin[(k_{za}-k_{zb})z]e^{-(\alpha_{za}+\alpha_{zb})z}\left(\frac{\alpha_{xa}}{\omega\mu_1}-\frac{\alpha_{xb}}{\omega\mu_1}\right). \quad (12)$$

In such a case, the power density $\langle S_x\rangle$ decays exponentially in $\hat{x}$ but oscillates between positive and negative values along $\hat{z}$ due to the sinusoidal function. Although this might seem to be the reason for the negative energy stream to appear at the image plane, this is still not the case. Upon considering the contributions from all the evanescent waves from a line source, we find that no negative power is generated at the image plane. In order to see this, we take the field at the image plane [the same as Eqs. (2) and (3) with an extra $\exp(-i2k_xd_1)$ term in the integrand], and consider only the evanescent waves. Taking advantage of k_x being an even function of k_z, we write the fields produced by the evanescent waves only as

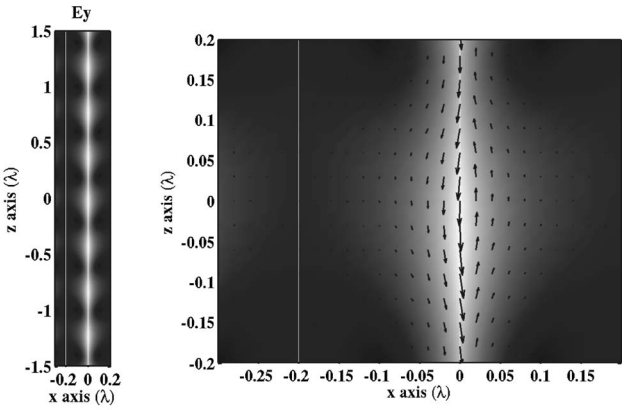

FIG. 8. Field and energy flux pattern of the interaction between a propagating wave and an evanescent wave in the presence of a LHM slab. The slab with a thickness of 0.2λ is between the white lines. The incident wave front is at 0.1λ in front of the slab. The plot shows that the negative-energy flux exist near the slab's second boundary after the evanescent wave is amplified by the LHM slab.

$$E_{y,\text{evan}}(z) = \frac{-\omega\mu_o}{2\pi}\int_{k_o}^{\infty} dk_z \frac{T(k_x)}{k_x} e^{i2k_x(d_2-d_1)}\cos k_z z, \quad (13)$$

$$H_{z,\text{evan}}(z) = \frac{-1}{2\pi}\int_{k_o}^{\infty} dk_z T(k_x) e^{i2k_x(d_2-d_1)}\cos k_z z. \quad (14)$$

For $k_z>k_o$, we have $k_x=\sqrt{(k_o^2-k_z^2)}=i\alpha_x$. Therefore, the term $T(k_x)e^{i2k_x(d_2-d_1)}\cos k_z z$ is real. Hence, $E_{y,\text{evan}}(z)$ is purely imaginary while $H_{z,\text{evan}}(z)$ is purely real, yielding no real power. A different way to see this is to examine Eq. (12) and to note that $\langle S_x\rangle$ is an odd function of $(k_{za}-k_{zb})$. After integrating over the symmetric spectrum of a line source, the integration of an odd function becomes zero.

The last case that remains to be considered is the interaction between evanescent waves and propagating waves. Again, starting from two waves with E_{ya} as a propagating wave and E_{yb} as an evanescent wave, the power along $\hat{x}$ is

$$\langle S_x\rangle = (1/2)\left\{\frac{k_{xa}}{\omega\mu_1}+\frac{k_{xa}}{\omega\mu_1}\exp\{-\alpha_{xb}x\}\cos[(k_{za}-k_{zb})z+k_{xa}x] + \frac{\alpha_{xb}}{\omega\mu_1}\exp\{-\alpha_{xb}x\}\sin[(k_{za}-k_{zb})z+k_{xa}x]\right\}, \quad (15)$$

which is no longer a simple odd function of $(k_{za}-k_{zb})$ as in Eq. (12). In addition, it can be seen that $\langle S_x\rangle$ can have negative values if $\exp(-\alpha_{xb}x)$ is compensated by the evanescent wave amplitude, which is made possible by LHM slabs. As a matter of fact, one of the interesting properties of LHM is to precisely amplify evanescent waves. For the purpose of illustration, we set up an incident propagating wave and an evanescent wave at the line-source location (Fig. 8), both with unit amplitude, to observe the power at the image plane. The wave vector in $\hat{z}$ for the propagating wave is $k_{za}=0.5k_o$ (where k_o is the free-space wave number), while the one for the evanescent wave is $k_{zb}=3k_o$. The fields of the slab configuration are solved analytically, and the amplitude of E_y is

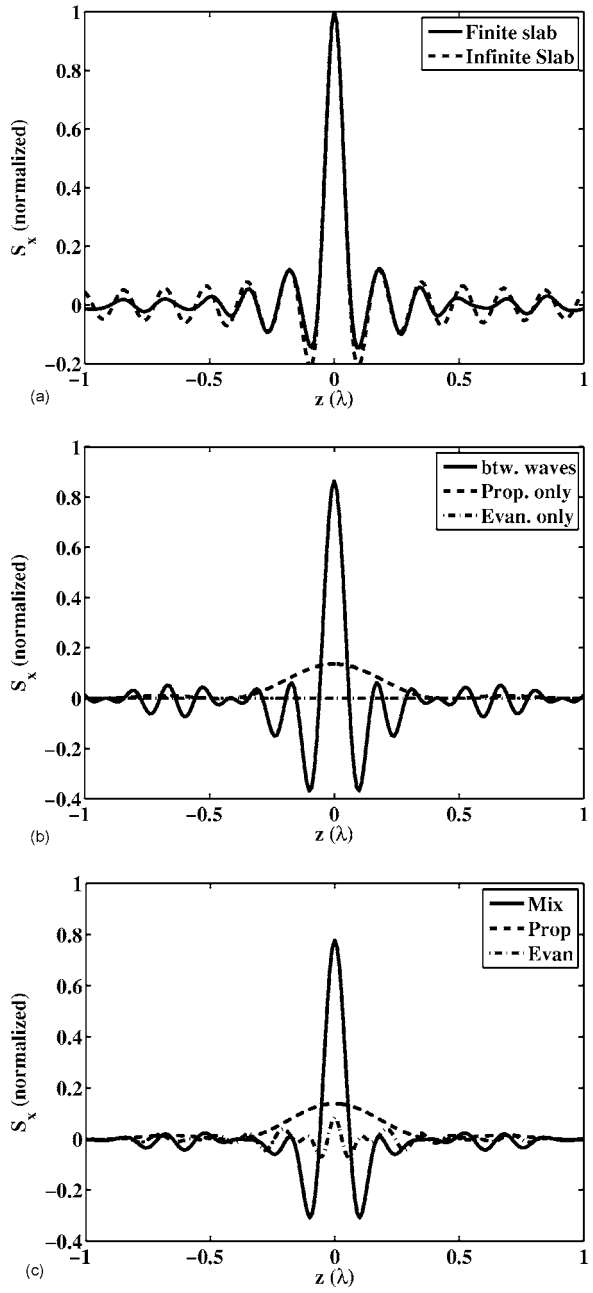

FIG. 9. Explanation of negative-energy streams in the LHM slab imaging. (a) Energy flux at the image plane from both an infinite slab and a finite slab. A negative-energy stream can be seen in both cases. (b) Contributions to the energy flux from wave interactions for the infinite slab. The fields are obtained analytically. (c) Contributions to energy flux from wave interactions for the finite slab. The fields are calculated from the FDTD simulation [(b) and (c)]. Solid line: interactions between propagating waves and evanescent waves; dashed line: propagating waves only; dot-dashed line: evanescent waves only.

shown in Fig. 8(a). At the slab's second boundary, large E_y amplitudes can be observed, which is due to the evanescent wave amplification inside the LHM slab. The oscillation in the field amplitude can be seen with a periodicity slightly greater than $\lambda/3$, which is close to the difference in the wave numbers of the two incident waves. Figure 8(b) shows a zoom-in view of the field and the time-averaged Poynting vectors in one spatial period along the z axis. Together with the field-amplitude oscillations, the Poynting power is also oscillating between positive and negative value in $\hat{x}$. Therefore, Fig. 8 illustrates that negative Poynting power can be obtained by the interactions between a propagating and an evanescent wave.

Further validation can be done in the case of a line source. The time-averaged Poynting power at the image plane from an infinite slab ($d_s=0.2\lambda$) is shown in Fig. 9(a). It can be seen that away from the central peak, the power oscillates between positive and negative values with a decaying amplitude. Decomposing the fields into propagating and evanescent waves, the contributions due to wave interactions can be evaluated, as is shown in Fig. 9(b). As expected, the propagating waves only contribute to the power in the positive direction, while the negative-energy stream comes from the interactions between propagating and evanescent waves. It also shows that the power due to the interaction of evanescent waves is zero.

Returning to the case of the finite-size slabs, we show that the same conclusion holds. The Poynting power at the image plane from the same finite-size slab used in the previous section ($d_s=0.2\lambda$, $L=2\lambda$) is shown in Fig. 9(a). Similar to the results from the infinite slab, negative time-averaged Poynting power can be observed. In order to study the contributions from the wave interactions, the time-domain field data at the image plane obtained from the FDTD simulations are first Fast-Fourier-transformed (FFT) into the frequency domain to verify the convergence. The data at the source frequency are then FFT from the spatial domain into the k space and a window function is applied to extract the propagating and evanescent waves. After being transformed back to the spatial domain by inverse FFT again, the wave interactions can be evaluated and the results are shown in Fig. 9(c). The contribution to the Poynting power from the evanescent waves is not exactly zero in this case, but it is much smaller compared to the contributions from other wave interactions. Similarly, the propagating waves only contribute to positive energy while the interactions between propagating and evanescent waves results in energy in the negative direction.

We emphasize again that the important reason for the negative-energy stream to be prominent at the image plane is the amplification of the evanescent waves inside the LHM slabs, which restores their amplitudes. Therefore, this phenomenon does not happen to right-handed material (RHM) slabs since the negligible evanescent wave energy due to the decay is overpowered by the energy from the propagating waves.

IV. CONCLUSION

In this paper, imaging properties of finite-size LHM slabs are analyzed. In particular, we use an approximate analytical method to study the effect of the finite size by considering only the aperture. It is shown that the approximated current sheet with a Gaussian shape truncated at the aperture repro-

duces the key features of the image spectrum. Hence the method can be used as a fast alternative to numerical simulations, although the simulations are still needed for a better accuracy. Furthermore, we explain that the negative-energy stream at the image plane comes from the inherent spectrum of the source, and more precisely from interactions between propagating waves and amplified evanescent waves inside LHM slabs. This phenomenon does not depend on the finite size of the slab.

ACKNOWLEDGMENTS

This work was sponsored by the Department of the Air Force under Air Force Contract No. F19628-00-C-0002, DARPA under Contract No. N00014-03-1-0716, the ONR under Contract No. N00014-01-1-0713, and by the Chinese National Foundation under Contracts No. 60371010 and No. 60531020.

[1] V. Veselago, Sov. Phys. Usp. **10**, 509 (1968).
[2] J. B. Pendry, Phys. Rev. Lett. **85**, 3966 (2000).
[3] D. R. Smith, W. J. Padilla, D. C. Vier, S. C. Nemat-Nasser, and S. Schultz, Phys. Rev. Lett. **84**, 4184 (2000).
[4] D. Smith, D. Schurig, M. Rosenbluth, and S. Schultz, Appl. Phys. Lett. **82**, 1506 (2003).
[5] M. Feise and Y. Kivshar, Phys. Lett. A **334**, 326 (2005).
[6] J. Lu, T. M. Grzegorczyk, B.-I. Wu, J. Pacheco, M. Chen, and J. A. Kong, Opt. Express **45**, 49 (2005).
[7] T. M. Grzegorczyk, C. D. Moss, J. Lu, X. Chen, J. P. Jr., and J. A. Kong, IEEE Trans. Microwave Theory Tech. **53**, 2956 (2005).
[8] J. J. Chen, T. M. Grzegorczyk, B.-I. Wu, and J. A. Kong, Opt. Express **13**, 10840 (2005).
[9] A. N. Lagarkov and V. N. Kissel, Phys. Rev. Lett. **92**, 077401 (2004).
[10] V. N. Kissel and A. N. Lagarkov, Phys. Rev. B **72**, 085111 (2005).
[11] L. Chen, S. He, and L. Shen, Phys. Rev. Lett. **92**, 107404 (2004).
[12] J. A. Kong, *Electromagnetic Wave Theory* (EMW, Cambridge, MA, 2000).
[13] W. C. Chew, Electromagn. Waves **51**, 1–26 (2005).